

FR3D: Three-dimensional Flow Reconstruction and Force Estimation for Unsteady Flows Around Arbitrary Bluff Bodies via Conformal Mapping Aided Convolutional Autoencoders

Ali Girayhan Özbay^a, Sylvain Laizet^a

^a*Department of Aeronautics, Imperial College London, Exhibition Road, London, SW7 2AZ, United Kingdom*

Abstract

In many practical fluid dynamics experiments, measuring variables such as velocity and pressure is possible only at a limited number of sensor locations, or for a few two-dimensional planes in the flow. However, knowledge of the full fields is necessary to understand the dynamics of many flows. Deep learning reconstruction of full flow fields from sparse measurements has recently garnered significant research interest, as a way of overcoming this limitation. This task is referred to as the flow reconstruction (FR) task. In the present study, we propose a convolutional autoencoder based neural network model, dubbed FR3D, which enables FR to be carried out for three-dimensional flows around extruded 3D objects with arbitrary cross-sections. An innovative mapping approach, whereby multiple fluid domains are mapped to an annulus, enables FR3D to generalize its performance to objects not encountered during training. We conclusively demonstrate this generalization capability using a dataset composed of 80 training and 20 testing geometries, all randomly generated. We show that the FR3D model reconstructs pressure and velocity components with a few percentage points of error. Additionally, using these predictions, we accurately estimate the Q-criterion fields as well lift and drag forces on the geometries.

Keywords: flow reconstruction, neural networks

PACS: 47.27, 47.80, 07.05

2020 MSC: 68T07, 76F65

1. Introduction and related work

Flow reconstruction (FR) involves the prediction of dense fields such as velocity based on sparse measurements. Since typical experiments in fluids involve only point measurements of the flow via simple and inexpensive methods such as pitot tubes, FR techniques can provide researchers additional insight into flows when more advanced techniques such as particle image velocimetry (PIV) are not available.

Various statistical tools have been developed for FR [1, 2], however substantial strides were made recently with the application of deep learning (DL) to the field [3, 4, 5]. Applications outside typical wind tunnel-like scenarios, such as reconstruction of atmospheric flows based on satellite imagery [6], have also been developed.

However, the applicability of even these recent approaches to practical scenarios is limited. The first obstacle is tackling multi-geometry FR. Even recently published works typically investigate FR for a single geometry only [7] (often a 2D circular cylinder), and as a result the models used in such works must be re-trained for every case investigated; a model trained on e.g. a circular cylinder will not work well for a square cylinder. This necessitates laborious data collection and a computationally expensive training process. To overcome this limitation, a growing body of works have investigated 2D multi-geometry FR using techniques such as graph convolutional neural networks [8, 9, 10] and conformal mappings [11].

The second challenge pertains to the reconstruction of three-dimensional flows, regarding which relatively few works exist compared to the reconstruction of two-dimensional flows. Three dimensional flows exhibit substantially more complicated dynamics than two-dimensional flows [12], and require much greater computing power to process. Despite this, a growing body of works is tackling the challenge of 3D FR. Particularly, reconstruction of 3D flows past cylinders [13] and of flows concerning domains without embedded objects such as channel flows [14, 15] have been investigated recently. A number of studies have also investigated the reconstruction of 2D slices of flows past square cylinders [16, 17] and vice versa [18] (i.e. reconstruction of 3D fields from 2D slices).

In this work, we introduce a method enabling the reconstruction of unsteady three-dimensional flows around objects with arbitrarily shaped cross-sections. This is achieved via an autoencoder-based convolutional neural network architecture which incorporates conformal mappings to achieve ge-

ometry invariance [11, 19]. In our previous study [19, 11], we have shown that it is possible to reconstruct dense contemporaneous or future vorticity fields of two-dimensional flows past arbitrary objects from current sparse sensor measurements, without geometry-specific training. To achieve optimal performance in these tasks, Schwarz-Christoffel mappings were used for choosing the sampling points of the dense fields. The results showed that the mapping aided approach provides a substantial boost in accuracy for all model and sensor setup configurations, enabling percentage errors under 3%, 10% and 30% for reconstructions of pressure, velocity and vorticity fields, respectively.

For the present study, we reconstruct unsteady three-dimensional flows around bluff bodies with periodic spanwise boundary conditions at $Re = 500$ (based on the freestream velocity and the characteristic length of the bluff body). Additionally, we use these reconstructions to accurately predict the aerodynamic forces experienced by the investigated geometries as well as the Q-criterion [20], which defines vortices as areas where the vorticity magnitude is greater than the magnitude of the rate of strain.

The paper is organized as follows: first, in Section 2, we detail the procedure used to generate our dataset and the experiments to be carried out using the dataset. Next, in Section 3, we expound upon the FR3D model architecture and its training procedure. Subsequently, in Section 4, we display the performance of the FR3D model. Finally, in Section 5, we summarize the results, and identify avenues for further research in 3D flow reconstruction.

2. Data and experimental setup

2.1. Geometries, meshing and flow simulations

Our dataset consists of 100 geometries $G_i, i \in [0, 99]$, randomly generated using a method based on Bezier curves by Viquerat et al. [21]. Each geometry uses 4 control points for the curves, chosen randomly in a square domain with characteristic length L_m , which enables the generation of convex as well as concave shapes. Figure 1 showcases the diversity of the geometries created in this manner, including airfoil-like cross-sections, objects with concavities and objects with sharp corners.

Each geometry G_i was placed in a $40L_m/7 \times 40L_m/7$ square domain, extruded for $20L_m/7$ in the spanwise direction. The domains were meshed using an automated procedure with c. 30,000 hexahedral and triangular prism elements each, with wake refinement applied. The flows were computed

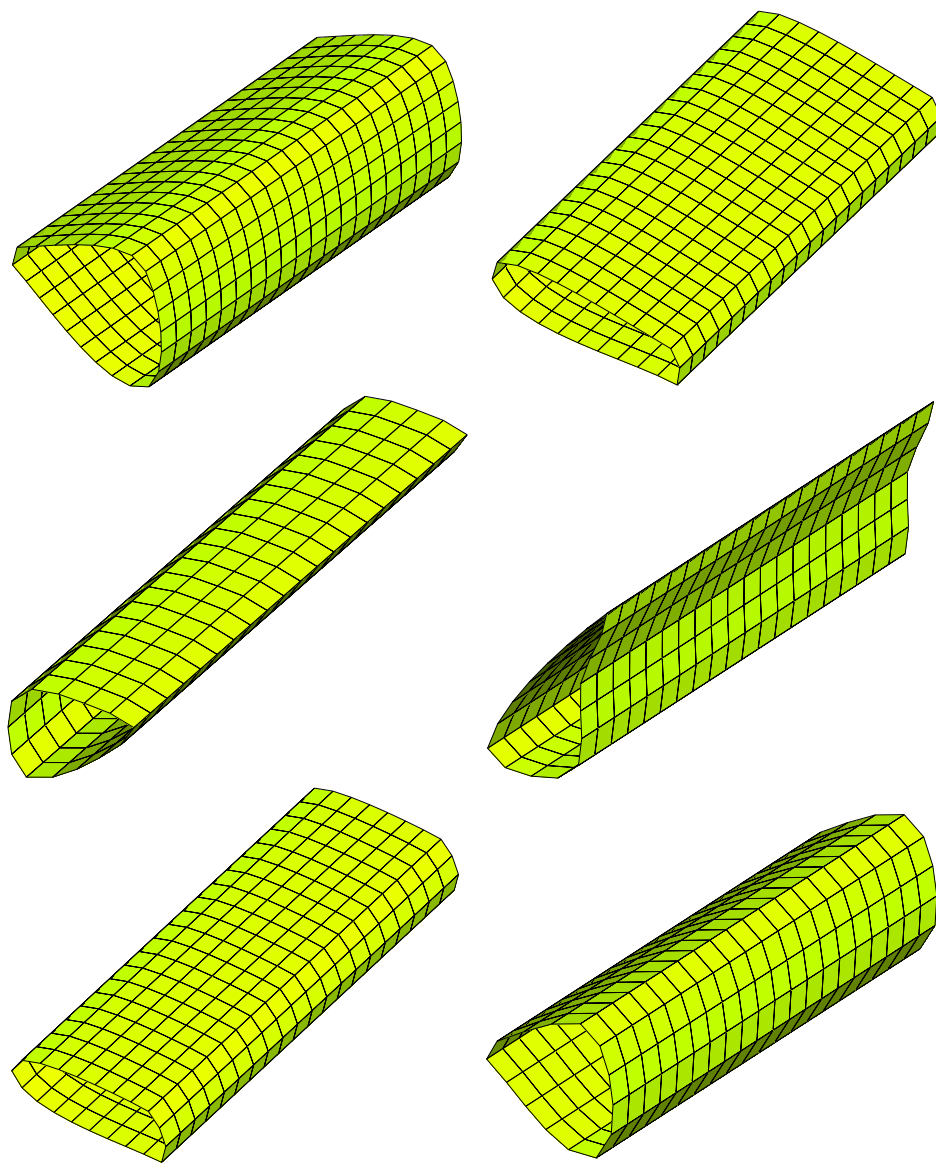


Figure 1: Surface meshes of a selection of the randomly generated geometries used in the study

at a Reynolds number equal to $\text{Re} = u_\infty L_m / \nu = 500$ using the PyFR solver [22] (u_∞ is the free stream velocity and ν is the viscosity of the flow). This solver is a flux reconstruction [23] based advection-diffusion equation solver using the artificial compressibility approach to solve the incompressible Navier-Stokes equations. It was chosen for its Python interface and GPU acceleration capabilities. 800 snapshots between $\tau^* = 5.71$ and $\tau^* = 17.14$ (when the flow is fully established) were recorded per geometry, where $\tau^* = u_\infty \tau / L_m$ is the time normalized by the large eddy turnover time L_m / u_∞ .

The snapshots collected were split into training and validation datasets, with all snapshots belonging to 20 randomly chosen geometries constituting the validation set, and the rest serving as the training set. This setup ensures that our model must have reasonable generalization performance to perform well on the validation set, as learning the reduced-order dynamics of specific flows (as in e.g. the Dynamic Mode Decomposition [24]) is not sufficient to reconstruct flows past unseen geometries.

2.2. Flow validation

The solver settings used to generate the flow dataset were validated using the canonical case of the flow past a cylinder with diameter D in a spanwise periodic domain. Two quantities were compared against reference data by Mittal and Balachandar [25] at $\text{Re} = 300$, both averaged in the spanwise direction:

- $\langle u \rangle - u_\infty$: Time averaged u -velocity deficit
- $\langle u' u' \rangle / u_\infty^2$: Streamwise-component of the Reynolds stress tensor

Our results were obtained using an automatically generated mesh, created with the same procedure as the one used to generate the meshes for the random geometries. The solver settings were kept identical to the settings used to obtain flow solutions for the random geometries, save for adjusting u_∞ to obtain the correct Reynolds number. The solution took approximately 1 hour to complete on a single Nvidia A100 GPU. The two quantities are plotted at several downstream locations in Figure 2.

The plots show good agreement between the reference values and our flow solution. u -velocity deficit profiles, including the peak deficit, are replicated with minimal errors at all three downstream locations. Streamwise Reynolds stress tensor results also show good agreement throughout most of the domain

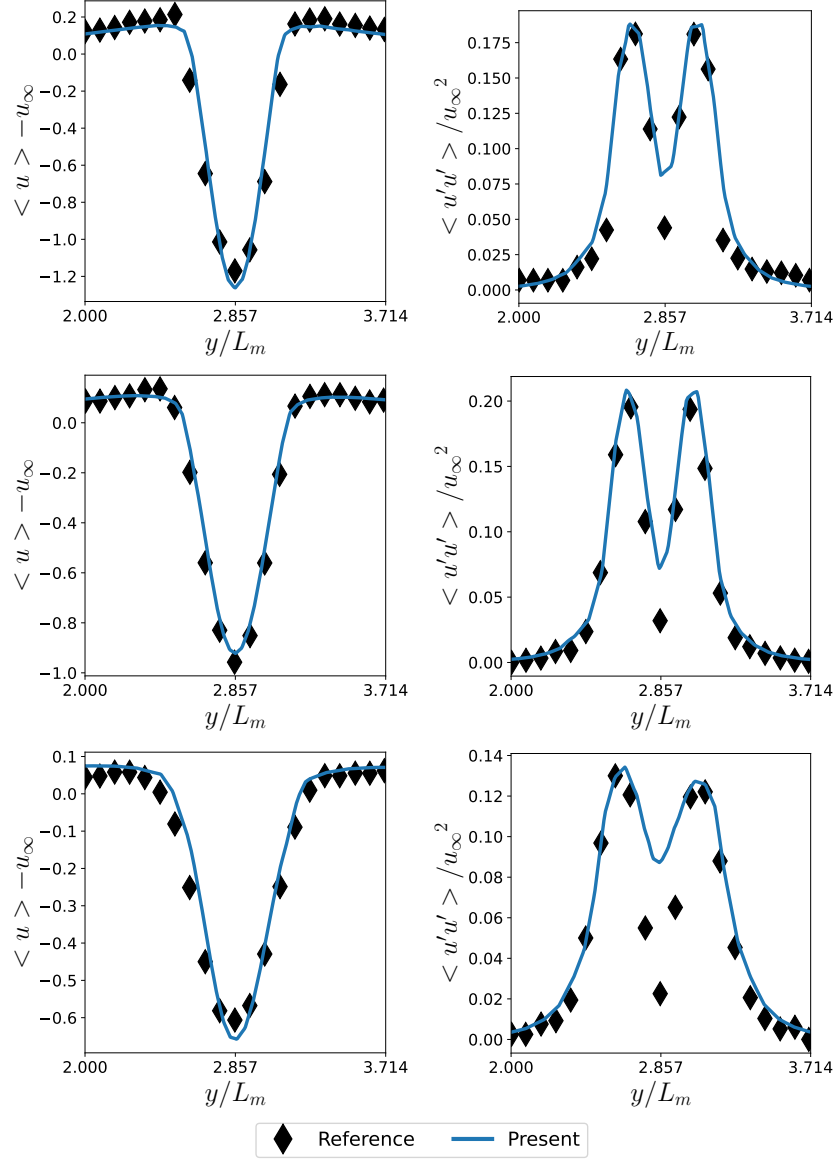


Figure 2: Comparison of results by Mittal and Balachandar [25] with our results for $\langle u \rangle - u_\infty$ (left) and $\langle u'u' \rangle / u_\infty^2$ (right) for the $Re = 300$ cylinder, $1.2D$ (top), $1.5D$ (middle) and $2.0D$ (bottom) downstream the centre of the cylinder.

- important features such as the dual peaks of the profile are closely followed
- although the dip between the two peaks is underestimated.

As a further soundness check, we also compared the time averaged lift coefficient (C_L) and drag coefficient (C_D) values obtained from our simulation with published data. We recorded a C_D value of 1.46, which is in line with the range of values between 1.22 and 1.50 in previous literature as compiled by Giannenas and Laizet [26], and a C_L of 2.8×10^{-5} – i.e. practically 0 for a single precision calculation – as expected. Thus, as our meshing and solver settings produce results that are largely in line with previous literature for this validation case, we can be confident that our dataset consists of physically correct snapshots.

2.3. Postprocessing

As the final step in our data generation process, postprocessing was applied to the snapshots to obtain sets of inputs and outputs used to train the neural network models. Our postprocessing extends the methodology which was used in our previous works based on conformal mappings to incorporate geometry invariance in neural network based FR methods [11, 19].

In the aforementioned method, the fluid domain F_i around each geometry G_i is treated as a doubly connected 2D region, and a mapping f between an annulus and F_i is computed, as visualized in Figure 3. Subsequently, a grid equispaced in the radial and angular dimensions is generated in the annular domain, and the mapping is used to calculate the coordinates of the gridpoints in F_i , which constitute the sampling points of the ground truth dense fields. As a result, each slice of the grid along the radial direction is guaranteed to start on the surface of the geometry G_i and end on the outer boundary of the fluid domain.

This work extends the method by incorporating the extrusion of the 2D cross section in the third dimension. In essence, this allows the dense flow fields around each geometry to be represented in cylindrical coordinates (r, θ, z) . We choose a resolution of 64 grid points per dimension; hence, the dense fields are sampled on a $64 \times 64 \times 64$ grid.

We consider two experiments with different types of sensor inputs. In the first experiment, the sensor inputs consist of pressure and velocity probes. The former consist of 50 probe locations equispaced in the angular direction along the inner ring in the annular domain at 10 stations equispaced in the spanwise direction, for a total of 500 pressure sensors. The latter, also consisting of 500 sensors, are arranged in a $10 \times 10 \times 5$ grid, spanning a $L_m \times$

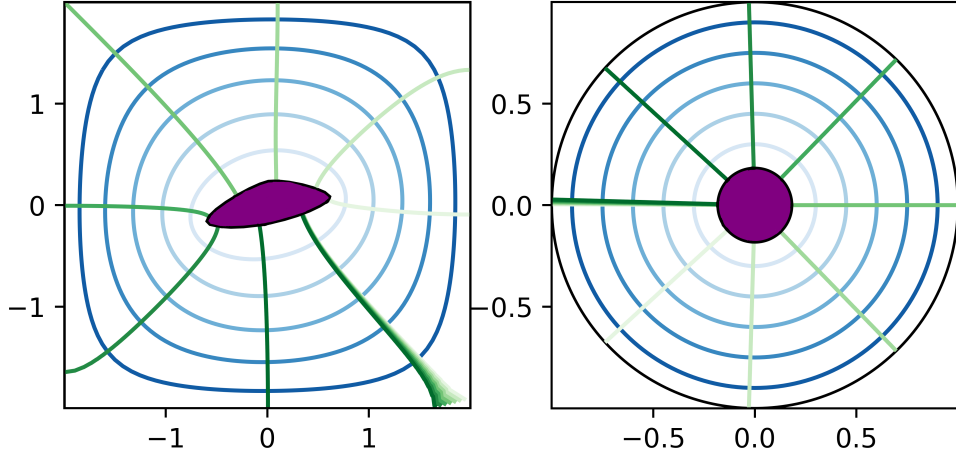


Figure 3: A random geometry (left) and its corresponding preimage (right). Blue and green contours depict the norm and argument in the annular domain, respectively.

$5L_m/3 \times 20L_m/7$ box $L_m/7$ downstream of the trailing edge of each object. Using this setup, dubbed the "sparse" setup, we consider the reconstruction of the four primary variables in the Navier-Stokes equations – the pressure p and the three velocity components u, v and w .

The second experiment retains the previous pressure sensor setup but uses plane measurements of velocity fields, called the "plane" setup. Two perpendicular planes with 32×32 velocity sensors each are considered; an xy -plane and an xz -plane, both downstream of the randomly generated objects. This setup is of particular interest within the context of PIV, an optical technique used in experiments capable of only measuring velocities in a particular plane, for which the pressure fields must be inferred from the velocity measurements [27]. The two sensor setups are visualized in Figure 4.

3. Model architecture and training

To carry out 3D flow reconstruction, we use a convolutional autoencoder-based architecture, dubbed FR3D. The convolutional architecture was chosen due to similar architectures' strong relative performance in previous multi-geometry FR scenarios [11]. It consists of three parts: an encoder, a decoder and a latent embedder. The encoder

$$\mathcal{E} : \mathbb{R}^I \rightarrow \mathbb{R}^L$$

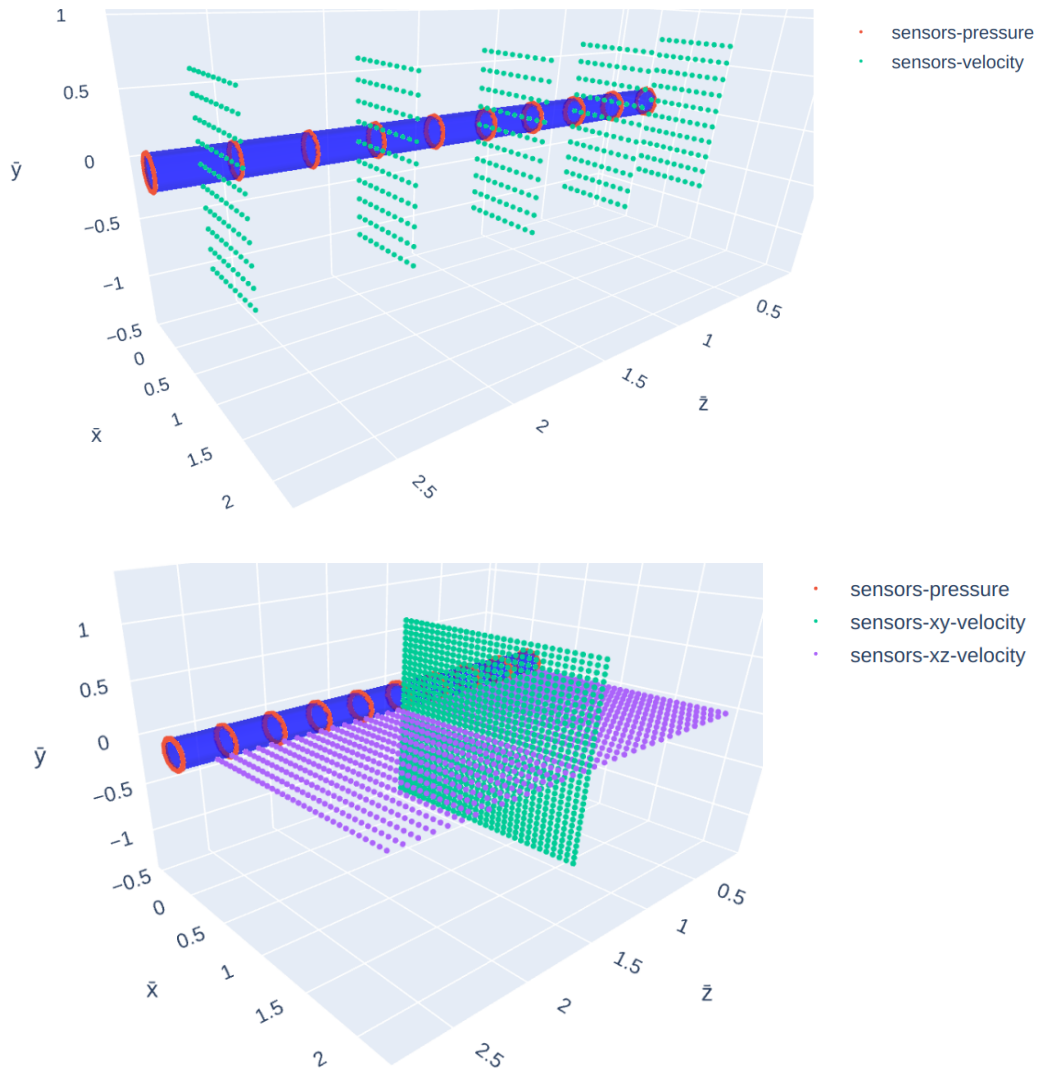


Figure 4: 3D representation of the sparse (top) and plane (bottom) sensor setups on a circular cylinder. $\bar{x}, \bar{y}, \bar{z}$ refer to the x, y, z coordinates normalized by L_m .

Table 1: Parameter counts of the overall FR3D model and its submodels in the sparse sensor configuration.

	Submodel parameters	Total parameters
Encoder	124,910,960	
Decoder	128,917,481	402,163,801
Latent embedder	148,335,360	

compresses its input \mathbf{x} into a latent space embedding \mathbf{l} , where $I \ll L$. Its architecture is a typical convolutional encoder architecture; each block consists of an initial convolution to double the number of channels, followed by sub-blocks applying batch normalization [28], a further convolution and a residual (skip) connection [29] to the beginning of the sub-block, and finally downsampling via average pooling. Our setup involved four such blocks, with four sub-blocks per block. The activation function used for all intermediate convolutional layers is the leaky rectified linear unit (LeakyReLU)

$$\text{LeakyReLU}(x) = \max(\alpha x, x).$$

After the encoder, the decoder

$$\mathcal{D} : \mathbb{R}^L \rightarrow \mathbb{R}^I$$

de-compresses \mathbf{l} into an approximation $\hat{\mathbf{x}}$ of \mathbf{x} . The decoder is similar to the encoder in structure, except the downsampling operations are replaced with upsampling operations via transpose convolutions.

In order to make the autoencoder useful for the flow reconstruction task, a further submodel

$$\mathcal{L} : \mathbb{R}^S \rightarrow \mathbb{R}^L$$

is necessary, which we call the latent space embedder. The latent space estimates latent space embeddings $\hat{\mathbf{l}}$ from the the sensor inputs \mathbf{s} , which may be then used to compute $\hat{\mathbf{x}}$. It consists of a dense layer and several convolutional layers. The overall FR3D architecture is summarized in Figure 5, and the parameter counts are displayed in Table 1.

The training of the autoencoder was conducted using the ADAM optimization algorithm with an initial learning rate of 10^{-4} . For each batch in the dataset, an optimization step is taken for the weights of \mathcal{E} and \mathcal{D} . Then, the weights of the decoder are 'frozen' and a further optimization step is taken

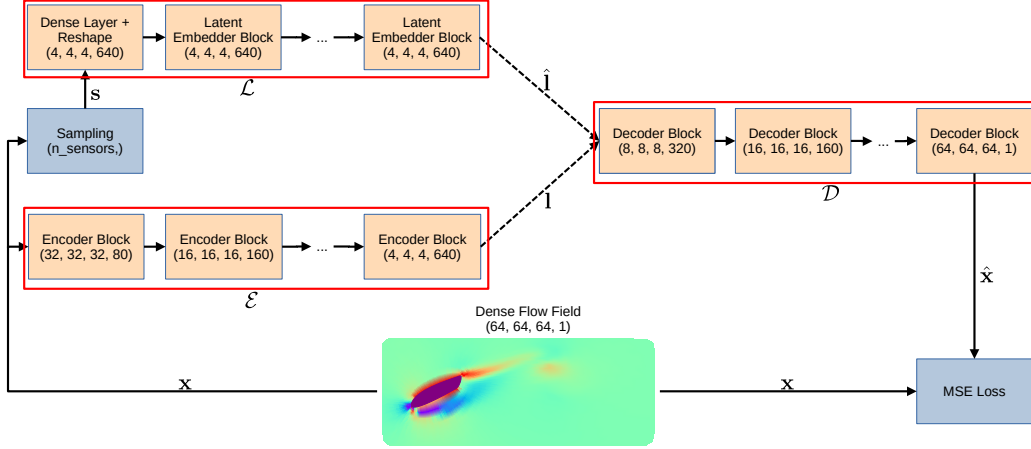


Figure 5: Our model architecture for 3D flow reconstruction. The integer tuples in each block indicate the shape of the tensor outputted by that block. The first three dimensions correspond to the spatial dimensions, and the final dimension is the channel dimension.

for \mathcal{L} . This procedure, involving the dense field \mathbf{x} , the sensor inputs \mathbf{s} and the weights $\mathbf{w}_E, \mathbf{w}_D, \mathbf{w}_L$ of $\mathcal{E}, \mathcal{D}, \mathcal{L}$ respectively, is summarized in Algorithm 1.

Algorithm 1 Optimization of the FR3D model using a single batch of data

```

1: function OPTIMIZE( $\mathbf{w}_E, \mathbf{w}_D, \mathbf{w}_L, \mathbf{s}, \mathbf{x}$ )
2:    $\mathbf{l} := \mathcal{E}(\mathbf{x}, \mathbf{w}_E)$ 
3:    $\hat{\mathbf{x}} := \mathcal{D}(\mathbf{l}, \mathbf{w}_D)$ 
4:    $\mathbf{w}_E \leftarrow \text{ADAM}(\nabla_{\mathbf{w}_E} L(\mathbf{x}, \hat{\mathbf{x}}), \mathbf{w}_E)$ 
5:    $\mathbf{w}_D \leftarrow \text{ADAM}(\nabla_{\mathbf{w}_D} L(\mathbf{x}, \hat{\mathbf{x}}), \mathbf{w}_D)$ 
6:    $\hat{\mathbf{l}} := \mathcal{L}(\mathbf{s}, \mathbf{w}_L)$ 
7:    $\hat{\mathbf{x}} \leftarrow \mathcal{D}(\hat{\mathbf{l}}, \mathbf{w}_D)$ 
8:    $\mathbf{w}_L \leftarrow \text{ADAM}(\nabla_{\mathbf{w}_L} L(\mathbf{x}, \hat{\mathbf{x}}), \mathbf{w}_L)$ 
9: end function

```

The models and the training procedure were implemented using Tensorflow [30] version 2.9 running on a server with two Nvidia A100 40GB GPUs and an AMD EPYC 7443 24-core CPU. The number of training epochs was determined using an early stopping mechanism based on the validation loss, which automatically stops training when the validation loss level does not decline after a set number of epochs. To expedite the training process, once

the weights of \mathcal{E} and \mathcal{D} were obtained during training for the sparse sensor setup, they were reused for the plane sensor setup. The procedure was carried out separately for all flow variables (pressure p and velocity components u, v, w), each taking approximately 48 hours to converge.

4. Results

Below, we present the results obtained by applying the FR3D model trained using the procedure in Section 3 to the validation dataset, consisting of 20 geometries not encountered during training. First, we display the results obtained for reconstructing the pressure and velocity from sparse sensors in Section 4.1, with Q-criterion contours also accurately reconstructed from the predicted velocity fields. Next, we demonstrate that the FR3D model can also be extended to estimate pressure fields from velocity data sampled on perpendicular planes in Section 4.2. Finally, we demonstrate that the pressure and velocity predictions from the FR3D model can be used to accurately estimate the time evolution of the drag and lift coefficients in Section 4.2.1.

4.1. Reconstruction from sparse sensors

We begin our analysis of the results using the sparse sensor case. Table 2 provides an overview of the model’s overall performance via the mean absolute percentage error (MAPE) and mean squared error (MSE) metrics averaged over the entire validation dataset. To focus on the regions of highest interest in the domain, the error metrics are computed for sampling points inside a box with extents $[-L_m, 8L_m/3] \times [-L_m, L_m]$ in the x - and y -directions relative to the centroid of each object and covering the entire spanwise direction.

Table 2: Mean absolute percentage (MAPE) and mean squared (MSE) error levels achieved by the FR3D model on the validation dataset for reconstruction from sparse sensors. The "Input to \mathcal{D} " column refers to whether the model was run with the sensors (using the latent embedder submodel \mathcal{L} , inference configuration) or the ground truth field (using the encoder submodel \mathcal{E}) as the inputs.

Var.	Input to \mathcal{D}	MAPE ¹	Min-max MAPE ²	MSE	Min-max MSE
p	\mathcal{L}	9.50%	6.33%	1.33×10^{-2}	2.19×10^{-3}
	\mathcal{E}	3.68%	2.34%	1.86×10^{-3}	3.07×10^{-4}
u	\mathcal{L}	5.05%	2.71%	4.53×10^{-3}	7.91×10^{-4}
	\mathcal{E}	3.71%	1.73%	2.02×10^{-3}	3.34×10^{-4}
v	\mathcal{L}	19.74%	3.74%	4.77×10^{-3}	8.65×10^{-4}
	\mathcal{E}	14.21%	1.83%	1.48×10^{-3}	2.47×10^{-4}
w	\mathcal{L}	35.06%	4.42%	2.09×10^{-3}	1.52×10^{-3}
	\mathcal{E}	33.75%	2.78%	1.11×10^{-3}	6.90×10^{-4}

The error figures show that, overall, our model generalizes well to the validation set. The raw MAPE values for p and u are both below 10% for previously unseen geometries, which is in line with our previous work with 2D geometries [19, 11], despite the substantially greater challenge of 3D flows which contain more complicated structures orientated in various directions. In terms of absolute errors and normalized percentage errors, the predictions for v and w are also at a similar level of accuracy. However, we draw attention to the large discrepancy between MAPE and Min-max MAPE figures for v and w . This is caused by the fact that, due to our choice of boundary conditions, the mean ground truth values for p and u are distributed around a mean of 1, while those of v and w are distributed around 0. Due to this, though the absolute error levels (i.e. the numerator of the percentage error expression) are broadly similar for all four variables, the percentage error metrics for v and w are much higher since the denominator of the percentage error expression is much smaller for those variables.

Figures 6, 7 and 8 provide further qualitative insights into the strong per-

¹Percentage error figures are filtered to remove gridpoints with ground truth values less than 2% of the maximum absolute ground truth value in a snapshot

²"Min-max" refers to error figures with min-max normalization applied based on the ground truth field.

formance of the model via iso-contours of the Q-criterion, iso-contours of the pressure, and slices of both pressure and velocity components (respectively), for three randomly chosen snapshots exhibiting varying degrees of spanwise effects. 3D visualisations of these quantities from experimental data are often difficult as previously discussed – e.g. the amplification of sensor noise when computing velocity gradients presents a serious challenge for plotting the Q-criterion from experimental measurements. Thus, our results lay the groundwork for a step-function improvement in visualisation of results from fluid dynamics experiments via flow reconstruction, all without the need for complicated post-processing techniques.

The contour plots indicate that the model is able to reconstruct the key details of the flow field. Most important features to focus on are the shed vortices downstream of the object, and the streamwise structures. The shed vortices’ locations and intensities are correctly reconstructed in all three cases, as shown in the Q-criterion contours; we draw special attention to the correct prediction of the breakdown of the furthest downstream vortex in the third snapshot. Larger scale streamwise structures are also accurately reconstructed, particularly the hairpin structure in the first snapshot and the finger-like structures connecting the two shed vortices in the second snapshot. Hence, our model is capable of replicating flows with different intensities of spanwise effects, which manifest as streamwise aligned vortices, spanwise aligned vortices, or a combination of both.

Pressure contours in Figure 7 corroborate the observations from Q-criterion contours; the first two pressure snapshots display that the model is capable of reconstructing three dimensional features (the chimney-like structure in the first snapshot and the hole in the second snapshot) of the pressure field, while the third snapshot shows that the location and intensity of the shed vortices are correctly replicated. However, two areas of improvement stand out in both contour plots: first, compared to the ground truth, the predicted surfaces are noisier and less smooth. Second, some flow features at smaller length scales are missing; this is pronounced especially for the first snapshot in the figures.

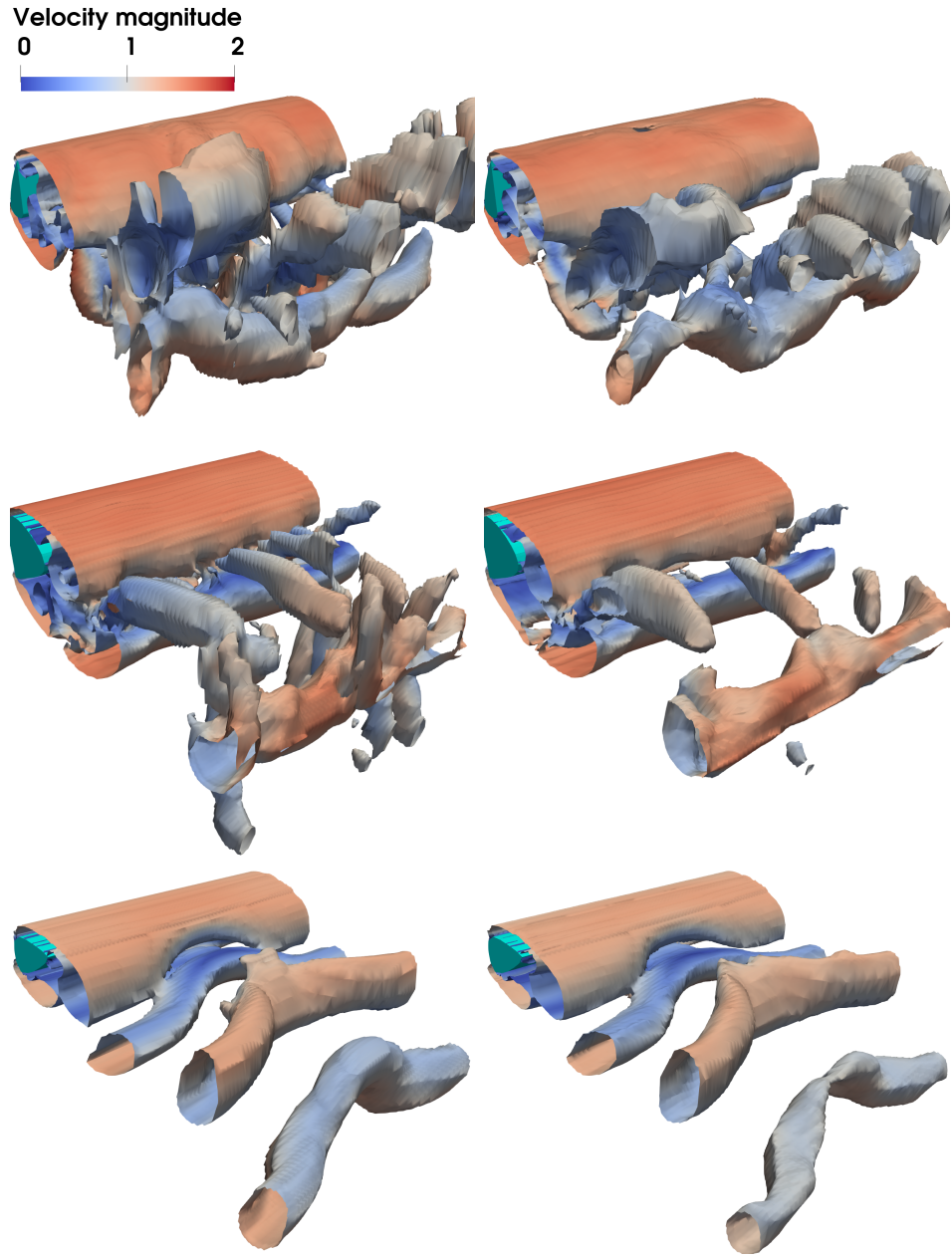


Figure 6: Ground truth (left) and predicted (right) Q -criterion ($Q = 0.05$) iso-contours from three randomly chosen snapshots belonging to different geometries.

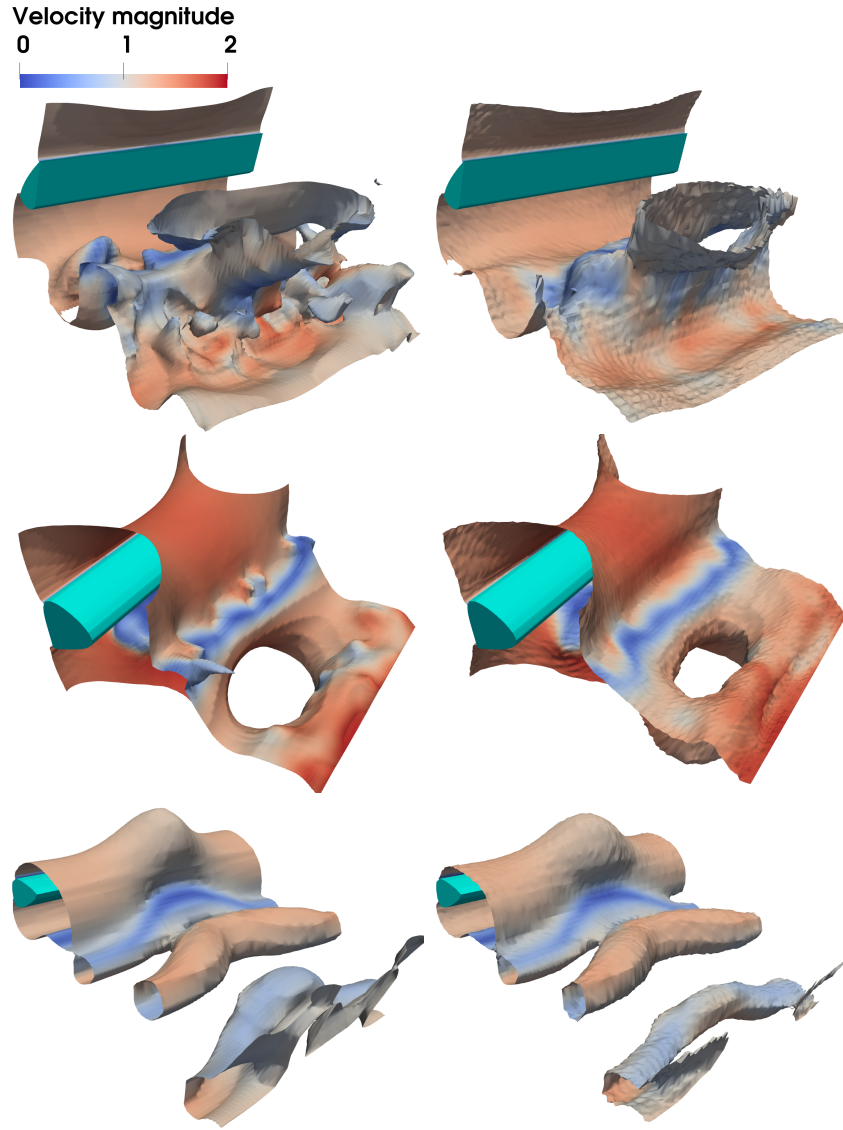


Figure 7: Ground truth (left) and predicted (right) pressure (top, bottom: $p = 0.85$, middle: $p = 0.75$) iso-contours coloured by velocity magnitude from three randomly chosen snapshots belonging to different geometries, using the model trained on the sparse sensor setup.

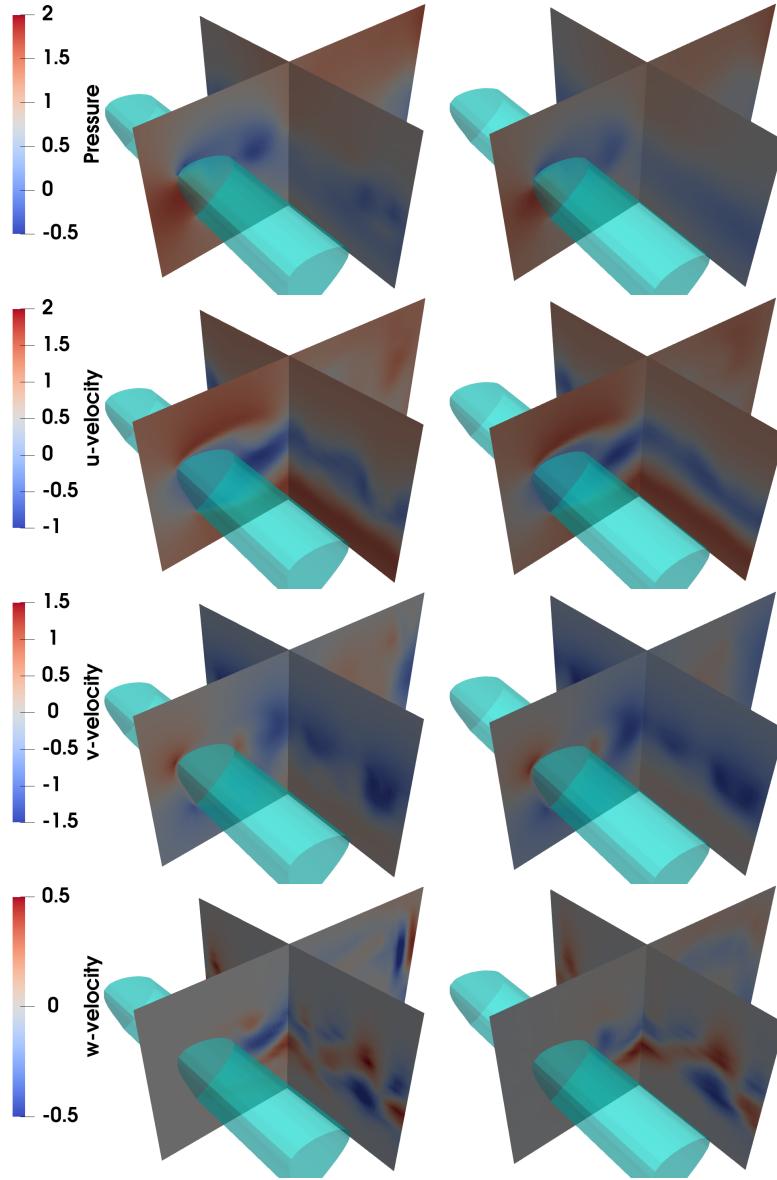


Figure 8: Ground truth (left) and predicted (right) slices of pressure and velocity fields for the middle snapshot in Figures 6 and 7.

Complementing the contour plots, Figure 8 provides greater detail regarding the middle snapshot in Figures 6 and 7, which is depicting a spanwise vortex that has just been shed from the trailing edge of the object, connected via streamwise structures to a second spanwise vortex further downstream. The core of the newly shed vortex in the snapshot is reconstructed clearly as shown by the xy -planes of the p and u plots, identifiable by the low pressure region in the p plot and the recirculation region in the u plot. Meanwhile, the yz -planes of the v and w provide further evidence of the high quality of the reconstructed streamwise structures; the negative v regions and the rapidly alternating w regions are accurately reconstructed and correspond to the finger-like structures observed in Figure 6.

4.2. Reconstruction from plane measurements

Next, we showcase the results using the plane sensor setup. Table 3 displays error metrics with this sensor setup, similar to Table 2 for the sparse sensor setup. The error levels of p, u, w are slightly higher overall with this sensor setup, with the largest relative rise in error encountered in predictions of u , though the accuracy of predictions of v are slightly better. The similarity between the error levels of the plane setup and the error levels with the sparse setup demonstrates the flexibility of our model in regards to the sensor setup, which is highly important for its future potential applications since its main envisioned future use—physical experiments—can involve widely varying sensor setups.

Table 3: Mean absolute percentage (MAPE) and mean squared (MSE) error levels achieved by the FR3D model on the validation dataset for reconstruction from plane velocity measurements. Error metrics using the encoder input are not provided, as they are identical to the values in Table 2.

Var.	Input to \mathcal{D}	MAPE	Min-max MAPE	MSE	Min-max MSE
p	\mathcal{L}	10.19%	6.55%	1.46×10^{-3}	2.35×10^{-3}
u	\mathcal{L}	7.76%	5.17%	6.91×10^{-3}	9.66×10^{-4}
v	\mathcal{L}	18.15%	3.08%	4.56×10^{-3}	8.42×10^{-4}
w	\mathcal{L}	38.24%	5.77%	2.42×10^{-3}	2.33×10^{-3}

Pressure contours for three further geometries, using predictions made for this sensor setup, can be found in Figure 9. Similar to the pressure contour results for the sparse sensor setup in Figure 7, major features of the pressure field are accurately reconstructed with this sensor setup as well. Recovering pressure from plane measurements of velocity is often a challenge in experimental settings involving PIV [27]. Thus, the present results suggest the FR3D model has the potential to help overcome challenges associated with recovering pressure fields from PIV experiments.

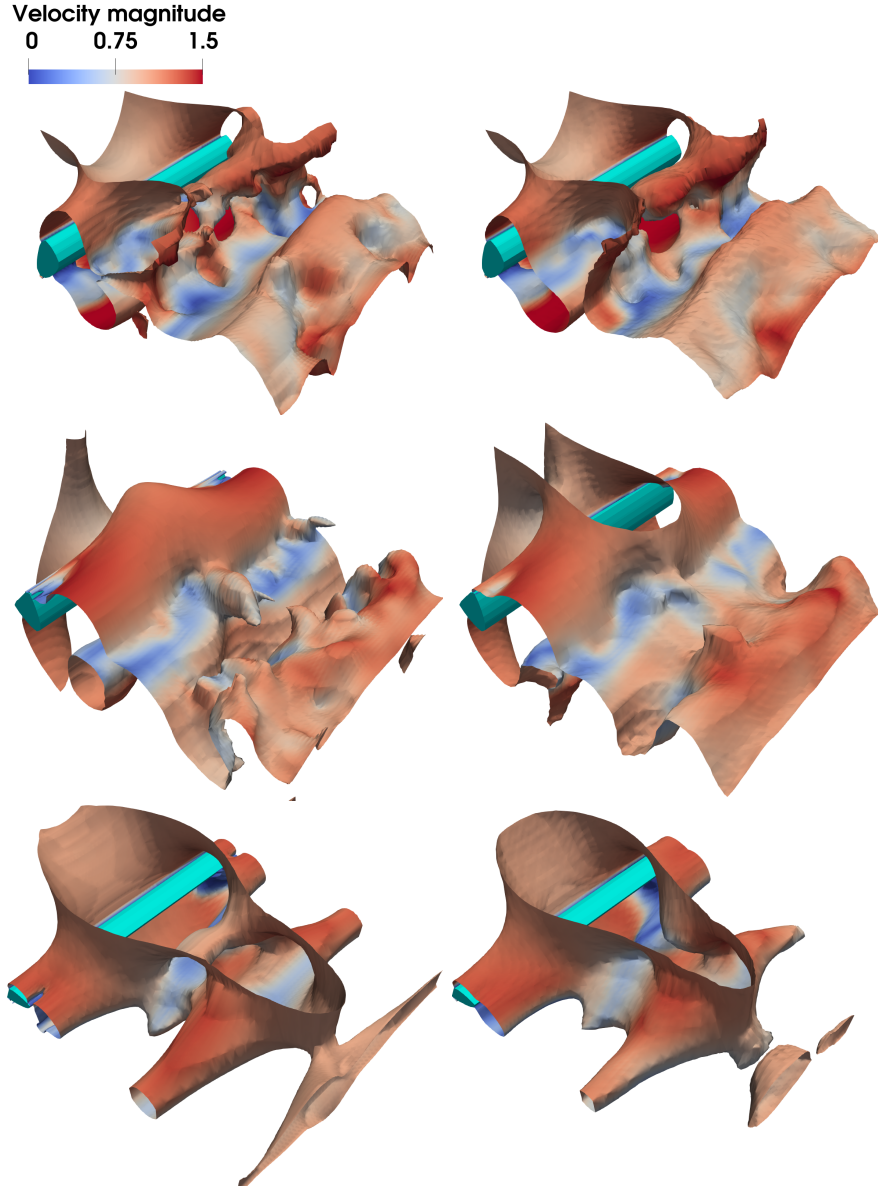


Figure 9: Ground truth (left) and predicted (right) pressure (top: $p = 0.75$; middle, bottom: $p = 0.85$) iso-contours coloured by velocity magnitude from three randomly chosen snapshots belonging to different objects, using the model trained on the plane sensor setup.

4.2.1. Estimation of lift and drag

Since the FR3D model is capable of accurately reconstructing the pressure and velocity fields, these results can be also applied to estimate the instantaneous lift and drag coefficients C_L and C_D experienced by the investigated geometries. Our choice of sampling points, utilizing the aforementioned conformal mapping approach instead of the more traditional Cartesian approach, makes this task substantially easier, as the need for interpolating the pressure and velocity fields onto the object surfaces is removed. This is due to the fact that the sampling points which lie on the inner ring of the annulus (cf. Figure 3) always lie on the original geometry's surface when the conformal mapping is applied.

To compute lift and drag forces, we adopt the approach of computing the body forces (pressure force and skin friction) through the integration of the pressure and the shear stresses across the object surface. The integration is carried out through the finite element method, approximating the surface of the geometry as a collection of quadrilateral surfaces. The dense field sampling points which lie on the object surface serve as the vertices of each quadrilateral. Since we do a simple extrusion in the z-direction, each quadrilateral is a rectangle. Defining a Cartesian coordinate system (ξ, η) on the quadrilateral, with the origin on one of the vertices of the quadrilateral, the standard bilinear basis functions

$$\begin{aligned} N_1 &= (1 - \xi)(1 - \eta), \quad N_2 = \xi(1 - \eta), \\ N_3 &= (1 - \xi)\eta, \quad N_4 = \xi\eta, \end{aligned}$$

can be used to approximate the pressure distribution on quadrilateral j as

$$\tilde{p}_j = \sum_i \hat{p}_{ij} N_i,$$

where \hat{p}_{ij} is the pressure prediction on vertex i of quadrilateral j . Consequently, the pressure force on the quadrilateral (with surface normal $\hat{\mathbf{n}}_j$) can be approximated by integrating \tilde{p}_j along the surface of the quadrilateral:

$$\vec{f}_{p,j} = \int \tilde{p}_j \hat{\mathbf{n}}_j \, dA. \quad (1)$$

For a rectangle, the result of Equation 1 is simply the average of the pressure values at its vertices, times its area

$$\vec{f}_{p,j} = \hat{\mathbf{n}}_j A_j \sum_{i=1}^4 \frac{1}{4} \hat{p}_{ij} = \vec{A}_j \sum_{i=1}^4 \frac{1}{4} \hat{p}_{ij}. \quad (2)$$

In practice, \vec{A}_j can be directly computed by taking the cross product of the vectors which run along the edges of the rectangle, and these vectors can be easily computed given the rectangle’s vertex coordinates. The overall pressure force can be computed by adding the pressure force on each quadrilateral $\vec{f}_p = \sum_j \vec{f}_{p,j}$.

The skin friction force \vec{f}_f can be computed by repeating the above procedure, substituting the wall shear stresses for the pressures. The shear forces can be approximated using the standard formula

$$\mu \frac{\partial u_{||}}{\partial n},$$

where μ is the dynamic viscosity, $u_{||}$ is the velocity parallel to the surface and n is the coordinate normal to the surface. The gradient term can be approximated as

$$\frac{\partial u_{||}}{\partial n} \approx \frac{u_{||}(n = \delta n) - u_{||}(n = 0)}{\delta n} = \frac{u_{||}(n = \delta n)}{\delta n} \quad (3)$$

The annular sampling method also greatly simplifies the computation of the approximation in Equation 3, as it ensures that each sampling point on the object surface (slice index 0 across the first dimension of the $64 \times 64 \times 64$ prediction array) has a corresponding sampling point above it in the wall-normal direction (slice index 1 across the first dimension of the same array).

Once both the skin friction forces \vec{f}_f and pressure forces \vec{f}_p are known, the overall body forces can be simply computed as $\vec{f} = \vec{f}_f + \vec{f}_p$. This method, combined with the FR3D model, leads to very accurate lift and drag predictions as seen in the error metrics averaged over the entire test dataset in Table 4 and the time evolutions of C_L and C_D plotted for two of the random test geometries in Figure 10.

The lift and drag estimation capability presented by the FR3D model presents a substantial leap over similar approaches in previous literature; for example, Chen et al. [8] demonstrated the capability to predict C_D with percentage errors of 3.43%, but only for steady 2D flows at Reynolds number equal to 10. In comparison, our model is capable of achieving similar levels of error, but for unsteady 3D flows for Reynolds numbers 50 times larger. The results are especially impressive when using the plane sensor setup, where we match the drag error levels reported by Chen et al. [8], despite the substantially more difficult task at hand.

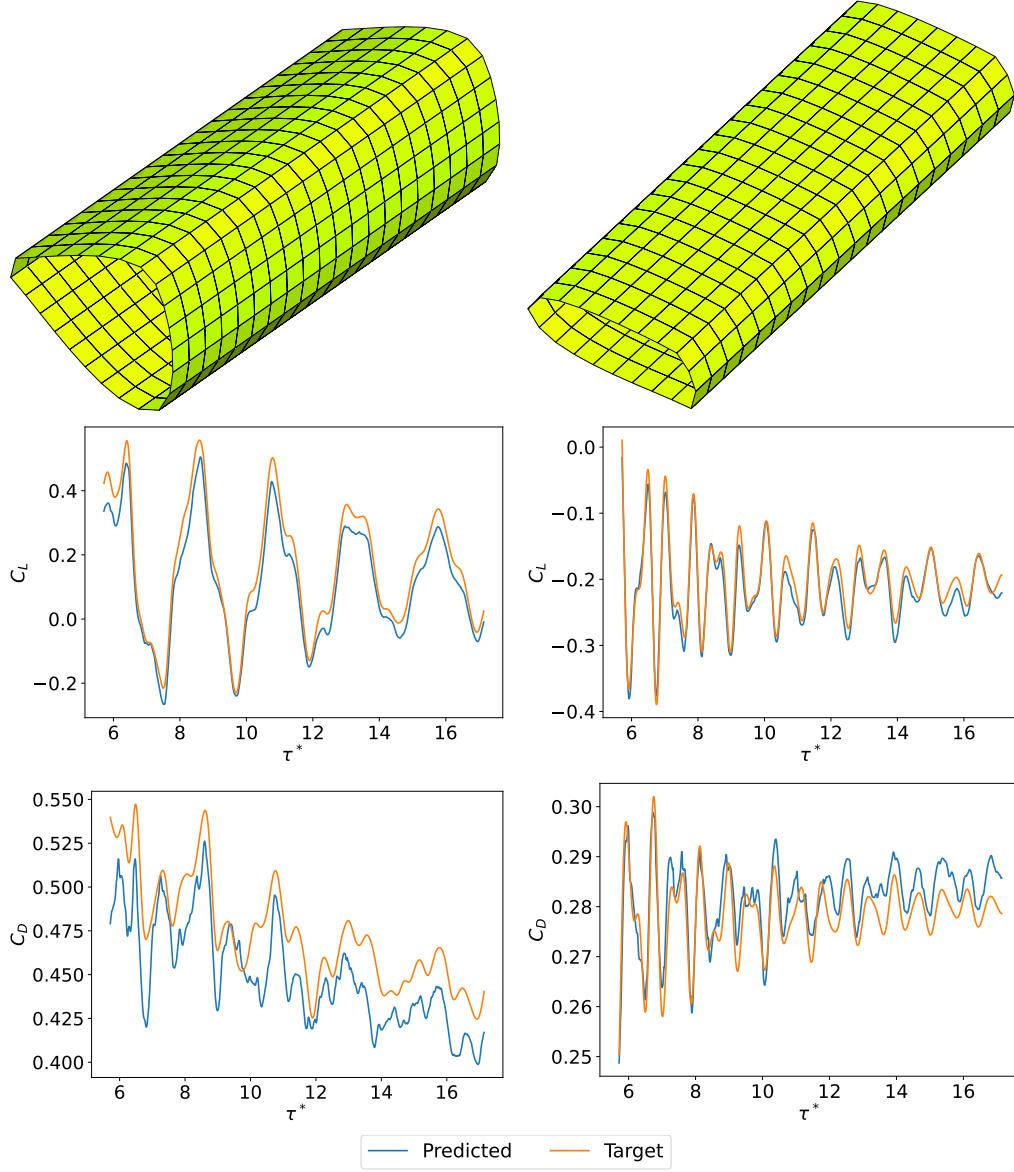


Figure 10: Time evolutions of the lift (middle) and drag (bottom) coefficients for two of the random geometries (left and right) in the test dataset. Predictions were made using the model trained using the sparse sensor setup, and the target values were computed using the body force results outputted by PyFR.

Table 4: Mean absolute percentage error (MAPE) and mean squared error (MSE) metrics averaged over the test dataset.

Sensor setup	Coefficient	MAPE	MSE
Sparse	C_L	9.16%	9.91×10^{-4}
	C_D	4.31%	4.86×10^{-4}
Planes	C_L	7.18%	6.91×10^{-4}
	C_D	3.43%	2.77×10^{-4}

We observed that our lift and drag predictions are especially accurate on high aspect ratio shapes resembling airfoils, such as the geometry on the right column in Figure 10. The level of accuracy on bluff bodies is still reasonably high, as seen in the bluff body on the left column in the same figure. However, we did see a slight degradation in accuracy on shapes with concave sections, such as the middle right geometry in Figure 1 for which the time-averaged C_L and C_D prediction errors were 14% and 8% respectively. This is due to the substantially more complicated flow patterns occurring in such geometries, and the relative rarity of such geometries in the dataset.

5. Conclusion and future work

In this study, we described the performance of FR3D, a convolutional autoencoder neural network model, on the reconstruction of three-dimensional flows past objects with varying cross-sections, given measurements of the flow field from sparse sensors and plane measurements. Using a conformal mapping technique to achieve geometry invariance, we demonstrated that the FR3D architecture is capable of reconstructing instantaneous pressure and velocity fields of flows past such geometries with min-max normalized percentage error levels under 10% for geometries not encountered during training at a fixed Reynolds number. The reconstructions are of a quality sufficient to accurately replicate the major features of Q-criterion and pressure iso-contours.

Subsequently, we applied the FR3D model to a scenario commonly encountered in experimental fluid dynamics involving PIV, whereby it is attempted to recover the flow variables – including pressure – from the measurements of the velocity components across two perpendicular planes downstream of the object. The FR3D model performed well also in this additional

scenario, reconstructing the dense pressure fields with percentage errors just above 10%.

Finally, using the reconstructed fields, we demonstrated that the lift and drag coefficients can be estimated within 10% of the ground truth values using both sensor setups, going as low as 3.43% when estimating drag coefficients using the plane measurement setup.

In the future, we aim to extend this work by investigating:

- **Noisy measurements:** The FR3D model was trained and evaluated using high-fidelity values obtained via computation. In contrast, a large degree of uncertainty exists in real-world measurements and ensuring that FR models are robust to noise will be necessary before they can be utilized in real laboratory environments, as opposed to computational studies.
- **More complex geometries:** The present work focused on investigating only objects extruded in the spanwise direction, in order to leverage our previous work on applying Schwarz-Christoffel mappings for training a model that can handle different geometries well. Different mapping techniques, such as boundary conforming curvilinear coordinate systems [31], or different neural network model architectures such as graph neural networks that do not depend on regular grids, will be necessary to achieve geometry invariance for a broader class of objects.
- **Varying Reynolds numbers:** Since the dataset in this work consisted solely of flows at a fixed Reynolds number, the model is not expected to perform well at other Reynolds numbers. Extending the model to perform well for a wide range of Reynolds numbers, possibly through adding a ‘physics-informed’ loss function component, will greatly boost its usefulness.
- **State-of-the-art generative models:** Recent advances in generative models for images, such as Diffusion architectures [32], constitute promising directions for substantial advances in flow reconstruction.

6. Acknowledgements

This work was supported by a PhD scholarship by the Department of Aeronautics, Imperial College London, and an Academic Hardware Grant by NVIDIA.

References

- [1] J. P. Bonnet, D. R. Cole, J. Delville, M. N. Glauser, L. S. Ukeiley, Stochastic estimation and proper orthogonal decomposition: complementary techniques for identifying structure, *Experiments in fluids* 17 (5) (1994) 307–314.
- [2] J. L. Callaham, K. Maeda, S. L. Brunton, Robust flow reconstruction from limited measurements via sparse representation, *Phys. Rev. Fluids* 4 (2019) 103907.
- [3] N. B. Erichson, L. Mathelin, Z. Yao, S. L. Brunton, M. W. Mahoney, J. N. Kutz, Shallow neural networks for fluid flow reconstruction with limited sensors, *Proceedings of the Royal Society A: Mathematical, Physical and Engineering Sciences* 476 (2238) (2020) 20200097. [arXiv:https://royalsocietypublishing.org/doi/pdf/10.1098/rspa.2020.0097](https://royalsocietypublishing.org/doi/pdf/10.1098/rspa.2020.0097).
- [4] P. Dubois, T. Gomez, L. Planckaert, L. Perret, Machine learning for fluid flow reconstruction from limited measurements, *Journal of Computational Physics* 448 (2022) 110733.
- [5] M. Morimoto, K. Fukami, K. Zhang, K. Fukagata, Generalization techniques of neural networks for fluid flow estimation, *Neural Computing and Applications* 34 (5) (2022) 3647–3669.
- [6] L. Schweri, S. Foucher, J. Tang, V. C. Azevedo, T. Günther, B. Solenthaler, A physics-aware neural network approach for flow data reconstruction from satellite observations, *Frontiers in Climate* 3 (2021).
- [7] S. Xu, Z. Sun, R. Huang, D. Guo, G. Yang, S. Ju, A practical approach to flow field reconstruction with sparse or incomplete data through physics informed neural network, *Acta Mechanica Sinica* 322302–.
- [8] J. Chen, E. Hachem, J. Viquerat, Graph neural networks for laminar flow prediction around random two-dimensional shapes, *Physics of Fluids* 33 (12) (2021) 123607. [arXiv:https://doi.org/10.1063/5.0064108](https://doi.org/10.1063/5.0064108).
- [9] Q. Liu, W. Zhu, F. Ma, X. Jia, Y. Gao, J. Wen, Graph attention network-based fluid simulation model, *AIP Advances* 12 (9) (2022) 095114.

- [10] G. Duthé, I. Abdallah, S. Barber, E. Chatzi, Graph neural networks for aerodynamic flow reconstruction from sparse sensing (2023).
- [11] A. G. Özbay, S. Laizet, Deep learning fluid flow reconstruction around arbitrary two-dimensional objects from sparse sensors using conformal mappings, *AIP Advances* 12 (4) (2022) 045126.
- [12] S. Verma, G. Novati, P. Koumoutsakos, Efficient collective swimming by harnessing vortices through deep reinforcement learning, *Proceedings of the National Academy of Sciences* 115 (23) (2018) 5849–5854.
- [13] S. Laima, X. Zhou, X. Jin, D. Gao, H. Li, Deeptnet: Time-resolved reconstruction of flow around a circular cylinder via spatiotemporal deep neural networks, *Physics of Fluids* 35 (1) (2023) 015118.
- [14] A. Güemes, S. Discetti, A. Ianiro, B. Sirmacek, H. Azizpour, R. Vinuesa, From coarse wall measurements to turbulent velocity fields through deep learning, *Physics of Fluids* 33 (7) (2021) 075121.
- [15] L. Guastoni, A. Güemes, A. Ianiro, S. Discetti, P. Schlatter, H. Azizpour, R. Vinuesa, Convolutional-network models to predict wall-bounded turbulence from wall quantities, *Journal of Fluid Mechanics* 928 (2021) A27.
- [16] T. Nakamura, K. Fukagata, Robust training approach of neural networks for fluid flow state estimations, *International Journal of Heat and Fluid Flow* 96 (2022) 108997.
- [17] M. Matsuo, T. Nakamura, M. Morimoto, K. Fukami, K. Fukagata, Supervised convolutional network for three-dimensional fluid data reconstruction from sectional flow fields with adaptive super-resolution assistance (2021).
- [18] J. M. Pérez, S. Le Clainche, J. M. Vega, Reconstruction of three-dimensional flow fields from two-dimensional data, *Journal of Computational Physics* 407 (2020) 109239.
- [19] A. G. Özbay, S. Laizet, Unsteady two-dimensional flow reconstruction and force coefficient estimation around arbitrary shapes via conformal mapping aided deep neural networks, in: *Proceedings of TSFP-12*, no. 195, 2022.

- [20] J. Jeong, F. Hussain, On the identification of a vortex, *Journal of fluid mechanics* 285 (1995) 69–94.
- [21] J. Viquerat, E. Hachem, A supervised neural network for drag prediction of arbitrary 2d shapes in laminar flows at low reynolds number, *Computers & Fluids* 210 (2020) 104645.
- [22] F. Witherden, A. Farrington, P. Vincent, Pyfr: An open source framework for solving advection–diffusion type problems on streaming architectures using the flux reconstruction approach, *Computer Physics Communications* 185 (11) (2014) 3028–3040.
- [23] H. T. Huynh, A flux reconstruction approach to high-order schemes including discontinuous galerkin methods, in: *18th AIAA computational fluid dynamics conference*, 2007, p. 4079.
- [24] P. J. Schmid, Dynamic mode decomposition of numerical and experimental data, *Journal of fluid mechanics* 656 (2010) 5–28.
- [25] R. Mittal, S. Balachandar, et al., On the inclusion of three-dimensional effects in simulations of two-dimensional bluff-body wake flows, in: *ASME fluids engineering division summer meeting*, Citeseer, 1997, pp. 1–6.
- [26] A. E. Giannenas, S. Laizet, A simple and scalable immersed boundary method for high-fidelity simulations of fixed and moving objects on a cartesian mesh, *Applied Mathematical Modelling* 99 (2021) 606–627.
- [27] R. De Kat, B. Van Oudheusden, Instantaneous planar pressure determination from piv in turbulent flow, *Experiments in fluids* 52 (5) (2012) 1089–1106.
- [28] S. Ioffe, C. Szegedy, Batch normalization: Accelerating deep network training by reducing internal covariate shift, in: *International conference on machine learning*, PMLR, 2015, pp. 448–456.
- [29] K. He, X. Zhang, S. Ren, J. Sun, Deep residual learning for image recognition, in: *2016 IEEE Conference on Computer Vision and Pattern Recognition (CVPR)*, 2016, pp. 770–778.

- [30] M. Abadi, P. Barham, J. Chen, Z. Chen, A. Davis, J. Dean, M. Devin, S. Ghemawat, G. Irving, M. Isard, et al., Tensorflow: A system for large-scale machine learning, in: 12th {USENIX} symposium on operating systems design and implementation ({OSDI} 16), 2016, pp. 265–283.
- [31] J. F. Thompson, General curvilinear coordinate systems, *Applied Mathematics and Computation* 10 (1982) 1–30.
- [32] R. Rombach, A. Blattmann, D. Lorenz, P. Esser, B. Ommer, High-resolution image synthesis with latent diffusion models, in: *Proceedings of the IEEE/CVF Conference on Computer Vision and Pattern Recognition*, 2022, pp. 10684–10695.